PAPER

Check for updates

3D hierarchical self-supported NiO/Co$_3$O$_4$@C/CoS$_2$ nanocomposites as electrode materials for high-performance supercapacitors†

Xingxing Zhu,[a] Mengyao Sun,[b] Rui Zhao,[a] Yingqi Li, [ID][ac] Bo Zhang,[a] Yingli Zhang,[a] Xingyou Lang, [ID][a] Yongfu Zhu [ID]*[a] and Qing Jiang [ID][a]

Multi-dimensional nanomaterials have drawn great interest for application in supercapacitors due to their large accessible surface area. However, the achievements of superior rate capability and cycle stability are hindered by their intrinsic poor electronic/ionic conductivity and the erratic structure. Herein, we develop a three-dimensional hierarchical self-supported NiO/Co$_3$O$_4$@C/CoS$_2$ hybrid electrode, in which NiO/Co$_3$O$_4$ nanosheets are *in situ* grown on a nickel foam substrate and combined with CoS$_2$ nanospheres through a carbon medium. The hybrid electrode has a high specific capacity of ∼1025 C g^{-1} at 1 A g^{-1} with a superior rate performance of ∼74% capacity retention even at a current density of 30 A g^{-1}. Moreover, the assembled NiO/Co$_3$O$_4$@C/CoS$_2$//AC hybrid supercapacitor achieves excellent performance with a maximum voltage of 1.64 V and a high energy density of 62.83 W h kg^{-1} at a power density of 824.99 W kg^{-1} and excellent cycle stability performance with a capacity retention of ∼92% after 5000 cycles. The high electrochemical performance of the hybrid supercapacitor is mainly attributed to the porous structure of the NiO/Co$_3$O$_4$@C nanosheets and CoS$_2$ nanospheres and intimate integration of active species. The rational strategy for the combination of various earth-abundant nanomaterials paves a new way for energy storage materials.

1. Introduction

Clean and sustainable energy storage devices have been highly pursued due to the urgent need to address the issues on air pollution and insufficient resource storage.[1–3] Among them, supercapacitors draw tremendous attention because they possess many appealing properties such as high power density, fast charge and discharge efficiency and long cycle life.[4,5] Generally, electrode materials can be divided into capacitive, pseudocapacitive and battery-type materials according to the charge storage mechanism. In contrast to the capacitive material that originates from the electrostatic accumulation of surface charge[6–8] and the pseudocapacitive materials that refers to the case involving a process of rapid reversible faradaic redox reaction near the electrode interface,[9–11] battery-type materials are able to deliver higher capacity by means of deep surface faradaic reactions.[12] Of them, battery-type materials have

attracted increasing attention due to their higher capacity and energy density. In general, the choice of electrode materials of supercapacitors can largely affect their electrochemical performance, including the cycling stability and reversibility in the reaction.[1,6]

Based on this, transition metal oxides/sulfides can be utilized as promising electrode materials in virtue of them being low-cost, environmentally friendly, and rich in valence states beneficial to the redox reaction.[13,14] As a typical transition metal oxide for a battery-type electrode material, NiO possesses outstanding electrochemical properties such as a theoretical specific capacity as high as 2584 F g^{-1}. However, NiO can only achieve relatively low capacity and compromise the rate capability due to its intrinsic high resistance nature.[15–17] Meanwhile, although the extensively reported transition metal sulfides, such as CoS$_2$,[18] NiS$_2$ [19] and MoS$_2$,[20] possess higher electronic conductivity and ability to achieve faster redox reaction relative to their oxide counterparts due to their large lattice gap and low band gap, the tendency of agglomeration during preparation greatly hinders the realization of high specific capacity. Moreover, large volume expansion and the resultant fast capacity decay also occur due to the irreversible reactions during repeated cycling.

To address the above issues, some studies attempted to combine oxides with sulfides as active materials for battery-type capacitors to improve the electrochemical performance, since

[a]Key Laboratory of Automobile Materials, Ministry of Education, School of Materials Science and Engineering, Jilin University, Changchun 130022, China. E-mail: yfzhu@jlu.edu.cn

[b]School of Materials Science and Engineering, Fudan University, Shanghai 200433, China

[c]College of Materials Science and Engineering, Jilin Jianzhu University, Changchun 130118, China

† Electronic supplementary information (ESI) available. See DOI: 10.1039/d0na00013b

such a nanocomposite can provide abundant defects and voids to facilitate the rapid transport of ions and kinetics of surface reaction at the oxide/sulfide interface.[21–23] In order to make use of their advantages, strategies of constructing novel core–shell structures are emerging, such as $NiCo_2O_4$@Ni–S,[24] Co_3O_4@-CoS,[25] $NiCo_2O_4$@$NiCo_2S_4$,[26] and $MnCo_2O_4$@CoS.[27] Meanwhile, the poor conductivity of oxides and instability of sulfides during long-term cycling can be effectively improved by introducing highly conductive carbonaceous materials, in virtue of their ability to enhance the charge transfer rate across the active material to the current collector and simultaneously provide buffer space for active sites. Therefore, constructing a transition metal oxide/sulfide nanocomposite with a highly conductive carbon medium is a rational way to improve the electrochemical performance of supercapacitors.

Considering the structure of electrode materials, two-dimensional (2D) materials have drawn tremendous attention in recent years due to their high and accessible surface area.[28,29] However, their surface area will be greatly reduced in the restacking process during synthesis. On the other hand, three-dimensional (3D) hierarchical structures have been widely used in energy storage because they can integrate the advantages of components, possessing large numbers of active sites.

Herein, we report a green and facile strategy to construct a novel nickel foam supported 3D hierarchical NiO/Co_3O_4@C/CoS_2 hybrid nanostructure as a positive electrode for supercapacitors. The 3D highly conductive nickel foam (NF) framework provides sufficient room for incorporating high-capacity NiO/Co_3O_4@C/CoS_2 nanocomposites. The *in situ* synthesis of NiO/Co_3O_4 nanosheets on NF through annealing of Ni–Co layered double hydroxide (LDH) avoids the involvement of insulating polymer binders commonly used in conventional capacitors, which can reduce the resistance and dead volume of the electrode system. The carbon modification enables the ultra-thin NiO/Co_3O_4@C nanosheets to act as a skeleton and conductive agent for CoS_2, which can avoid agglomeration of CoS_2 during the fabrication process. CoS_2 enables fast redox reactions and also provides a more accessible surface area and electroactive sites for achieving outstanding electrochemical performance. Benefiting from the synergistic effect of the constituents, the NiO/Co_3O_4@C/CoS_2 electrode has a specific capacity of 1025 C g^{-1} at 1 A g^{-1} and superb rate capability of 74% retention at 30 A g^{-1}. Hybrid supercapacitors based on the NiO/Co_3O_4@C/CoS_2 positive electrode and active carbon (AC) negative electrode exhibit outstanding cycling stability.

2. Experimental

2.1. Preparation of the NiO/Co_3O_4@C/CoS_2 hybrid electrode

Typically, nickel foam (50 mm × 20 mm × 1 mm) was washed sequentially with acetone, 3 M HCl solution, distilled water and absolute ethanol to ensure a clean surface. After cleaning, the nickel foam was immersed in a solution containing Ni(NO$_3$)$_2$·6H$_2$O (0.5 mmol), CoCl$_2$·6H$_2$O (0.5 mmol), CTAB (1 g), H$_2$O (20 mL) and methanol (20 mL) and placed in an oven at 180 °C for 24 h and then placed in a drying oven at 60 °C for 12 h to obtain Ni–Co LDH. Then, a piece of nickel foam covered with Ni–Co

LDH was immersed in a 2.5 mM glucose solution at 180 °C for 6 h, and then annealed at 400 °C for 4 h in a N$_2$ atmosphere to achieve carbon modification. Finally, the specimen was placed in a solution containing 0.03 M CoCl$_2$·6H$_2$O and 0.05 M Na$_2$S$_2$O$_3$ at 150 °C for 12 h. After washing with distilled water and drying at 60 °C, the NiO/Co_3O_4@C/CoS_2 nanocomposite was obtained. The mass loading of the NiO/Co_3O_4@C/CoS_2 nanocomposite in the nickel foam was about 1.6 mg cm^{-2}.

2.2. Materials characterization

The morphology and microstructure of the as-prepared electrode were characterized using a field emission scanning electron microscope (FESEM, JEOL JSM-6700F, 15 keV) and a transmission electron microscope (TEM, JEOL JEM-2100F, 200 keV). X-ray diffraction (XRD) patterns were studied using a D/max 2500pc diffractometer with Cu Kα radiation. X-ray photoelectron spectroscopy (XPS) was carried out using an ESCALAB Mk II (vacuum generator) spectrometer with an Al anode. Raman spectroscopy characterization was performed on a Renishaw Raman spectrometer using a wavelength of 532 nm with an intensity of 0.05 mW. The specific area and pore size distribution were determined by nitrogen adsorption and desorption using a Micromeritics ASAP 2020 analyzer.

2.3. Electrochemical measurements

All electrochemical properties were investigated at room temperature in 6 M KOH. For a three-electrode configuration, platinum foil and a saturated calomel electrode were used as the counter and reference electrode, respectively. When studying the electrochemical performance of the assembled hybrid supercapacitor, the as-prepared nickel foam supported NiO/Co_3O_4@C/CoS_2 was used as the positive electrode, while the inexpensive activated carbon (AC) electrode was used as the negative electrode. The AC electrode was obtained by coating nickel foam with AC powder, carbon black and polyvinylidene fluoride (PVDF) with a weight ratio of 85 : 10 : 5. Then, a homogeneous mixture was obtained with the addition of *N*-methylpyrrolidone (NMP). The resulting mixture was coated onto a clean piece of nickel foam and dried at 60 °C for 12 h in an oven. Cyclic voltammetry (CV), galvanostatic charge–discharge (GCD) and electrochemical impedance spectroscopy (EIS) measurements were performed on a CHI 660B electrochemical workstation (Shanghai CH Instrument Company, China), while cycling performance was studied in a Land battery test system.

3. Results and discussion

3.1. Characterization

As briefly illustrated in Fig. 1, the NiO/Co_3O_4@C/CoS_2 hybrid electrode was fabricated. Scanning electron microscopy (SEM) and high-resolution transmission electron microscopy (HRTEM) were carried out to investigate the morphology and microstructure of Ni–Co LDH, NiO/Co_3O_4@C and NiO/Co_3O_4@C/CoS_2 specimens. As shown in Fig. S1a and b,† Ni–Co LDH nanosheets are uniformly and homogeneously synthesized
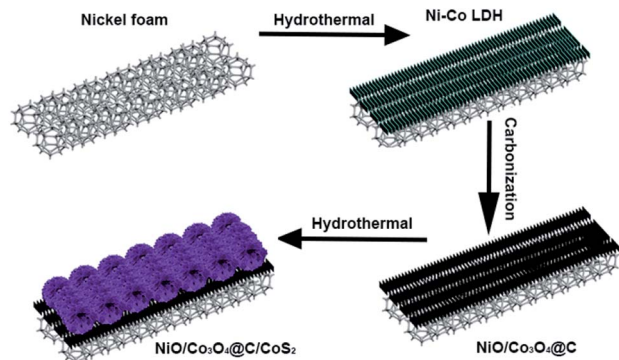
Paper

Fig. 1 Schematic illustration of the synthesis of 3D hierarchical NiO/Co_3O_4@C/CoS_2 hybrid nanostructure.

on the NF substrate, with a length of ∼600 nm and width of ∼270 nm as well as thickness of ∼25 nm. The vertically aligned nanosheets possess an anisotropic structure with a high surface-to-volume ratio, in favor of the access and transport of electrolyte ions. After carbon modification, no obvious change occurs in the morphology (Fig. S1c and d†). As shown in Fig. S1e,† the inter-planar spacing fringes with an interval of 0.24 and 0.21 nm are measured, corresponding to the (311) plane of cubic Co_3O_4 and the (200) plane of cubic NiO, respectively.[30,31] The intimate interface of vertically aligned NiO/Co_3O_4@C and the supported NF substrate ensure the possibility of the achievement of excellent stability and mechanical strength, which can be confirmed by Fig. S1f.†

Fig. 2a shows the SEM image of the 3D hierarchical NiO/Co_3O_4@C/CoS_2 specimen, where the CoS_2 nanospheres composed of ultrathin nanoflakes are uniformly anchored on
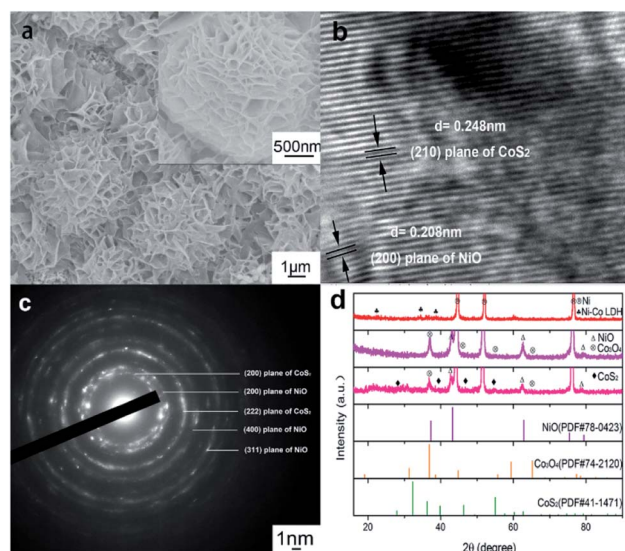
the NiO/Co_3O_4@C skeleton. As shown in Fig. S1g,† the morphology and thickness of NiO/Co_3O_4@C nanosheets, displayed in the black square, remain unchanged before and after the incorporation of CoS_2 nanospheres, indicating the robust structure of the NiO/Co_3O_4@C layer. Fig. 2b shows the HRTEM image of the 3D NiO/Co_3O_4@C/CoS_2 hybrid electrode. The measured lattice spacings of 0.208 nm and 0.248 nm are indexed to the (200) plane of cubic NiO and the (221) plane of cubic CoS_2, respectively. This indicates the coexistence of CoS_2 nanoflakes with NiO nanosheets and the existence of the crystal plane common lattice at the interface, as indicated by the black square in Fig. 2b. The corresponding selected area electron diffraction (SAED) pattern shown in Fig. 2c indicates the polycrystalline nature of the hybrid structure, and the definite diffraction rings can be easily indexed to (200), (400) and (311) planes of the NiO phase and (200) and (222) planes of the CoS_2 phase.

XRD characterization is applied to verify the crystallographic structure of Ni–Co LDH, NiO/Co_3O_4@C and NiO/Co_3O_4@C/CoS_2 samples shown in Fig. 2d. For the XRD pattern of Ni–Co LDH, except for the peaks from the NF substrate, all other characteristic peaks agree well with the Ni–Co LDH constituent. After carbon modification, obvious diffraction peaks emerge at 37.2°, 43.3°, 62.86°, 75.39°, and 79.38°, corresponding to (111), (200), (220), (311), and (222) planes of NiO (JCPDS file no. 78-0423), respectively. Meanwhile, the peaks located at 18.99°, 31.27°, 55.65°, 59.35°, and 82.62° are indexed to the (111), (220), (422), (511), and (444) planes of Co_3O_4 (JCPDS file no. 74-2120), respectively. The absence of any characteristic peak corresponding to carbon indicates its amorphous nature. In the incorporation process of CoS_2, the intensity of Co_3O_4 peaks weakens due to the chemical reaction of $8Co^{3+} + S_2O_3^{2-} + 5H_2O = 8Co^{2+} + 2SO_4^{2-} + 10H^+$. As shown in Fig. 2d, typical peaks of CoS_2 and NiO can be found in the XRD results of NiO/Co_3O_4@C/CoS_2, which is consistent with the result of SAED. Fig. S2† shows that the peaks of the corresponding main phases before and after the cycles are basically identical, indicating that the design of the layered structure is rational and stable.

Fig. S3† shows the EDS mapping analysis of the NiO/Co_3O_4@C/CoS_2 hybrid electrode. The elements of C, O, S, Co and Ni are distributed homogeneously over the electrode, which agrees well with the SEM and TEM results in Figs. 2 and S1,† indicating that the electro-active constituents obtained in each step are uniformly grown on the substrate. In order to prove the chemical composition of the nanocomposite, an XPS test is performed for the NiO/Co_3O_4@C/CoS_2 hybrid electrode.

Fig. 3a illustrates the characteristic peaks for nickel, cobalt, sulfur, oxygen and carbon in the full wide-scan spectrum. Using the C 1s peak with a binding energy of 284.6 eV as a calibration reference, the oxide and sulfide valence states of nickel and cobalt are analyzed through high-resolution XPS spectra of Ni 2p, Co 2p and S 2p shown in Fig. 3b. In the Ni 2p spectrum, the main peaks of Ni $2p_{3/2}$ and Ni $2p_{1/2}$ in the Ni 2p orbital can be respectively found at 855.85 eV and 873.7 eV with the spin–orbit splitting value at 15.9 eV, in accordance with standard NiO
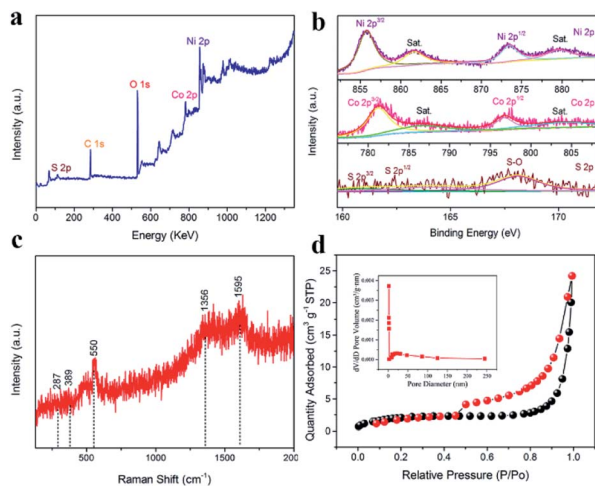

Fig. 2 (a) Typical SEM image of the multi-dimensional NiO/Co_3O_4@C/CoS_2 hybrid electrode; (b) HRTEM image of the multi-dimensional NiO/Co_3O_4@C/CoS_2 hybrid electrode; (c) typical SAED pattern of NiO/Co_3O_4@C/CoS_2; (d) XRD patterns of the NiO/Co_3O_4@C/CoS_2 sample before and after 5000 cycles, the bottom line patterns are the standard patterns of Ni, NiO, Co_3O_4 and CoS_2, respectively.

Fig. 3 (a) Clear wide scan XPS spectrum of the NiO/Co$_3$O$_4$@C/CoS$_2$ sample; (b) detailed high-resolution XPS spectra of the Ni 2p, Co 2p and S 2p of the NiO/Co$_3$O$_4$@C/CoS$_2$ sample; (c) Raman spectrum of the NiO/Co$_3$O$_4$@C/CoS$_2$ electrode material; (d) nitrogen adsorption–desorption isotherms and pore-size distribution (inset) of nickel foam coated with the NiO/Co$_3$O$_4$@C/CoS$_2$ sample.

peaks reported elsewhere.[31–33] Similarly, a high-resolution spectrum of Co 2p showed two major peaks at 779.4 eV for Co 2p$_{3/2}$ and 794.7 eV for Co 2p$_{1/2}$, consistent with previous studies.[34,35] Also, a high-resolution spectrum of S 2p exhibited a peak at 162.9 eV assigned to S$_2^{2-}$ of CoS$_2$. As for the peak located at 167.9 eV, it can be attributed to the chemical bond of S–O.[36] The O 1s spectrum (Fig. S4†) displayed three characteristic peaks of metal–oxygen bonds (529.9 eV for O1), defect sites with a low oxygen coordination (531.6 eV for O2), and hydroxyl groups (532.7 eV for O3). The higher O2 ratio of NiO/Co$_3$O$_4$@C/CoS$_2$ also indicated that NiO/Co$_3$O$_4$@C/CoS$_2$ possessed more oxygen vacancies than NiO/Co$_3$O$_4$@C.

Fig. 3c shows the Raman spectroscopy of the chemical composition of the hybrid electrode. There exist obvious peaks (~287, 389, 550, 1356 and 1595 cm^{-1}) in the wavenumber range of 100–2000 cm^{-1}, and the distinct peaks located at 1356 and 1595 cm^{-1} can be assigned to the disordered carbon (D-band) and the ordered graphitic carbon (G-band), respectively.[37–39] The peak located at 550 cm^{-1} is assigned to the longitudinal optical (LO) phonon modes of NiO,[39,40] while the peaks appearing at 287 and 389 cm^{-1} are attributed to the A$_g$ and E$_g$ modes of CoS$_2$,[41] consistent with the results of XRD characterization.

To further understand the detailed structural information, N$_2$ adsorption/desorption isotherms are measured at 77 K based on the Brunauer–Emmett–Teller (BET) method. Fig. 3d and S5† show the N$_2$ adsorption/desorption isotherms of nickel foam supported NiO/Co$_3$O$_4$@C/CoS$_2$ and NiO/Co$_3$O$_4$@C, respectively. The specimen of nickel foam supported NiO/Co$_3$O$_4$@C/CoS$_2$ possesses a surface area of 7.3297 m^2 g^{-1}, pore volume of 0.037 cm^3 g^{-1} and mean pore size of 12.537 nm, which are higher than those of nickel foam coated with NiO/Co$_3$O$_4$@C (a surface area of 3.5493 m^2 g^{-1}, pore volume of 0.0089 cm^3 g^{-1} and 12.266 nm). This confirms that the incorporation of CoS$_2$ nanospheres provides more accessible surface areas.

3.2. Electrochemical performances of the NiO/Co$_3$O$_4$@C/CoS$_2$ hybrid electrode

In order to evaluate the electrochemical performance of the NiO/Co$_3$O$_4$@C/CoS$_2$ hybrid electrode, cyclic voltammetry (CV) and galvanostatic charge–discharge (GCD) measurements were conducted in a three-electrode system. Fig. 4a shows the representative CV curves of the NiO/Co$_3$O$_4$@C/CoS$_2$ hybrid electrode (1 cm × 1 cm) at scan rates ranging from 1 to 20 mV s^{-1} in a potential window from −0.2 to 0.6 V. A pair of distinct symmetric cathodic/anodic peaks demonstrates the pseudo energy storage mechanism and the high reversibility during charging and discharging. This excellent performance can be also revealed by GCD measurements, whose profiles show a symmetrical triangular shape with similar charging and discharging time at the current densities ranging from 3 to 30 A g^{-1} (Fig. 4b). As illustrated in Fig. 4c, to further evaluate the rate capability of the hybrid electrode, the specific capacity under different current densities is calculated according to the following equation:[42]

$$Q = \frac{i\Delta t}{m}$$

At a current density of 1 A g^{-1}, the NiO/Co$_3$O$_4$@C/CoS$_2$ hybrid electrode achieves a high specific capacity of ~1025 C g^{-1} and maintains ~760 C g^{-1} (~74% retention) when the current density rises to 30 A g^{-1}, indicating its outstanding rate performance. Moreover, this high specific capacity in the whole range outperforms its Ni–Co LDH, CoS$_2$@C, CoS$_2$ and NiO@Co$_3$O$_4$@C counterparts (Fig. S6a†), which record
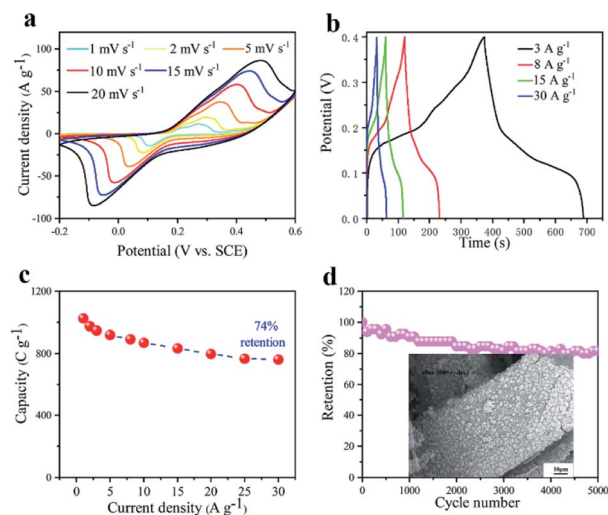

Fig. 4 Evaluation of the electrochemical performance of the as-prepared electrode based on a three-electrode cell. (a) CV curves of the NiO/Co$_3$O$_4$@C/CoS$_2$ NF electrode at different scan rates; (b) GCD curves of the NiO/Co$_3$O$_4$@C/CoS$_2$ NF electrode at different current densities; (c) rate performance of NiO/Co$_3$O$_4$@C/CoS$_2$ NF at various scan rates from 1 A g^{-1} to 30 A g^{-1}; (d) cycling stability over 5000 cycles of the NiO/Co$_3$O$_4$@C/CoS$_2$ electrode at a current density of 10 A g^{-1}; the inset shows the SEM image of the electrode after 5000 cycles.

a specific capacity of ~334, 387, 136 and 470 C g^{-1} at 1 A g^{-1}, respectively (Fig. S6b†). The cogent results prove that the introduction of the carbon layer can improve the reversibility of reactions and boost the electrochemical performance of constituent CoS_2, achieving large specific capacity and high coulombic efficiency.

The reasons for the high capacity as well as superb rate capability are explained mainly from the following aspects. Firstly, both vertically aligned NiO/Co_3O_4 nanosheets and CoS_2 nanospheres composed of ultrathin nanoflakes provide sufficient accessible active sites, ensuring highly efficient redox reactions in the electrode system. Secondly, the introduction of the carbon layer can effectively improve the electronic conductivity of oxides and protect the oxide skeleton during the annealing process. Thirdly, the synergistic effect of the oxide/sulfide nanocomposite can take advantage of the merits of each component. Furthermore, the achievement of the highest specific capacitance of the $NiO/Co_3O_4@C/CoS_2$ hybrid electrode relative to the other counterparts may be attributed to the reaction between Co_3O_4 and $Na_2S_2O_3$:[43,44]

$$2CoO \cdot Co_2O_3 \xrightarrow{Co_3O_4} 6Co'_{Co} + 3V_O^{\cdot\cdot} + 8O_o$$
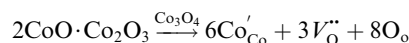
during which abundant oxygen defects and voids present along with Co^{2+} were formed on the surface of Co_3O_4, as illustrated in Fig. S7.† Furthermore, the reaction of a portion of Co_3O_4 has no influence on the structure of the homogeneous nanosheets that act as the bond of CoS_2, corresponding to Fig. S1g.† As the GCD curves show in Fig. S8,† the specific capacity of specimens with or without $Na_2S_2O_3$ is 588 and 470 C g^{-1}, confirming the contribution of the oxygen vacancies ascribed to the reaction between Co_3O_4 and $Na_2S_2O_3$. The cycling stability of electrodes is also a key criterion for supercapacitors. The hybrid electrode is cycled between 0 and 0.4 V at a high current density of 10 A g^{-1} for 5000 cycles, with the results shown in Fig. 4d. It demonstrates that the capacity retention of the $NiO/Co_3O_4@C/CoS_2$ hybrid electrode is ~81.5%, which is attributed to the rational design of carbon coating that accommodates the volume expansion of oxides/sulfides, the good mechanical strength of $NiO/Co_3O_4@C$ nanosheets, and the good adhesion between porous CoS_2 nanospheres and $NiO/Co_3O_4@C$ nanosheets. The SEM image of the hybrid electrode after cycling tests (inset of Fig. 4d) further confirms the stability of the electrode. To provide insight into the electrochemical behavior of the conductivity, Fig. S9† shows the Nyquist plot of the $NiO/Co_3O_4@C/CoS_2$ hybrid electrode with its equivalent circuit (inset). The internal resistance is as low as 0.5 Ω, which demonstrates the excellent capacitor characteristics of the device.

To further understand the charge storage mechanism of the $NiO/Co_3O_4@C/CoS_2$ hybrid electrode material, the electrochemical behavior can be analyzed according to the CV curves at small scan rates based on the equation of $\log I_p = b \log v + \log a$, wherein I_p (A) and v (mV s^{-1}) are the peak current and scan rate respectively, and a and b are the adjustable parameters. Both the surface capacitive effect and diffusion-controlled process play a role in the electrode material storage when the b-value is

in the range of 0.5–1.0. If the b-value is equal to 0.5, the battery-type properties dominate the electrochemical behavior. If the b value is equal to or greater than 1, the electrochemical behavior mainly rely on the pseudocapacitance properties and the surface capacitive effect. As shown in Fig. S10,† the b values of the anodic peak and cathodic peak are 0.5987 and 0.6768 respectively, indicating that the electrochemical behavior of the $NiO/Co_3O_4@C/CoS_2$ hybrid electrode is controlled by the surface capacitive effect and diffusion-controlled process.

3.3. Electrochemical performances of the $NiO/Co_3O_4@C/CoS_2$//AC hybrid device

To investigate the behavior of the $NiO/Co_3O_4@C/CoS_2$ electrode in a full-cell, as shown in Fig. S11,† a hybrid device is assembled by using $NiO/Co_3O_4@C/CoS_2$ as the cathode and AC as the anode (1 cm × 1 cm size). To achieve the maximum operation potential window, the electrode mass can be calculated according to the equation of $m_+/m_- = (C_-\Delta V_-)/(C_+\Delta V_+)$.[45,46]

To evaluate the electrochemical properties of this hybrid device, the CV measurements are carried out in a three-electrode system at 5 mV s^{-1}. The $NiO/Co_3O_4@C/CoS_2$ cathode is tested in a potential window of 0–0.6 V while the AC anode is tested between −1 and 0 V [47] (Fig. S12†). As shown in Fig. S13,† the AC electrode shows a specific capacitance of 147.9 C g^{-1} at 1 A g^{-1}. Fig. 5a shows the CV curves of the hybrid device at various scan rates ranging from 10 mV s^{-1} to 60 mV s^{-1}. The basically similar shape indicates the ability to store and deliver energy at high rates. Fig. S14† shows the GCD curves of the $NiO/Co_3O_4@C/CoS_2$//AC hybrid device at various current densities and that a stable working potential of 1.64 V can be achieved, which is much higher than 0.8–1.0 V of the traditional AC symmetrical supercapacitor, indicating the contribution of
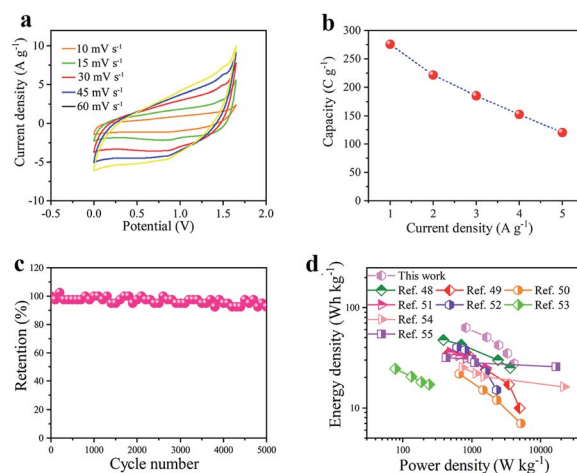

Fig. 5 Evaluation of the electrochemical performance of the $NiO/Co_3O_4@C/CoS_2$//AC hybrid device. (a) CV curves of the hybrid device at different scan rates; (b) rate performance of the $NiO/Co_3O_4@C/CoS_2$//AC hybrid device at various scan rates from 1 A g^{-1} to 5 A g^{-1}; (c) Ragone plots of the $NiO/Co_3O_4@C/CoS_2$//AC hybrid device and other reported data for comparison; (d) cycling stability over 5000 cycles of the $NiO/Co_3O_4@C/CoS_2$//AC hybrid device at a current density of 3 A g^{-1}.

transition metal oxides and sulfides. The specific capacity measured at various current densities based on the total mass of active materials in two electrodes is calculated, as shown in Fig. 5b. The specific capacity of ~274 C g^{-1} is achieved at 1 A g^{-1}.

In order to investigate the durability and long-term cycle stability of the hybrid device, Fig. 5c shows the capacity retention as a function of cycle time performed at a high current density of 3 A g^{-1}. It can be seen that the capacity can retain ~92% of its initial value after 5000 cycles. This result confirms the excellent rate capability and stability. Fig. 5d shows the comparison of the power/energy density for the NiO/Co$_3$O$_4$@C/CoS$_2$//AC hybrid device with those for recently reported works, such as NiCo$_2$O$_4$/NiO//AC,[48] NiCo$_2$O$_4$//AC,[49] Ni(OH)$_2$/nickel foam//AC,[51] Co(OH)$_2$/CoS$_2$//AC,[51] NiCo$_2$O$_4$/PANI//AC,[52] NiCo$_2$S$_4$@CoS$_2$//AC,[53] NiCo$_2$O$_4$/rGO hybrid//rGO,[54] and Co$_3$O$_4$ nanohorn//AC.[55] The NiO/Co$_3$O$_4$@C/CoS$_2$//AC device exhibits a high energy density of 62.83 W h kg^{-1} at a power density of 824.99 W kg^{-1}. This work is far superior to those of the reported data, illustrating the significant new prospect of 3D nanocomposites consisting of transition metal oxides/sulfides and carbon. In addition, we also compared important electrochemical properties with peer electrode materials shown in Table S1,† demonstrating the enhanced electrochemical properties. As aforementioned, the high performance of the NiO/Co$_3$O$_4$@C/CoS$_2$ structure is benefiting from the facilitation of rapid ion diffusion and fast electron transport, taking full advantage of oxides/sulfides and carbon materials and alleviating the corrosion of the active material by the electrolyte during charging and discharging.

The capacities of the hybrid electrode and hybrid device also can be calculated based on the following equation:

$$C = \frac{2i_m \int V \mathrm{d}t}{V^2|_{V_i}^{V_f}},$$

wherein $i_m = I/m$ (A g^{-1}) is the current density, I is the current, m is the active mass of the electrode, and $\int V \mathrm{d}t$ is the integral current area with V as the potential with initial and final values of V_i and V_f;[42] the rate performances of NiO/Co$_3$O$_4$@C/CoS$_2$ and NiO/Co$_3$O$_4$@C/CoS$_2$//AC are depicted in Fig. S15.†

To investigate the practical application of the device, Fig. S16† shows that two pieces of NiO/Co$_3$O$_4$@C/CoS$_2$//AC devices are connected in series to provide 3 V voltage in an electrolyte of 6 M KOH for 1 min. The six light-emitting diodes (LEDs) including two green (2.36 V, 20 mA), two yellow (1.80 V, 20 mA) and two red (1.76 V, 20 mA) LEDs could be lit at the same time by the devices.

4. Conclusions

In summary, a 3D hierarchical hybrid nanocomposite of NiO/Co$_3$O$_4$@C/CoS$_2$ has been successfully fabricated on a conductive nickel foam substrate via an in situ binder-free hydrothermal and annealing method to significantly elevate the specific capacity and improve the stability for supercapacitor

application. Benefiting from the combination of high-capacity oxide/sulfide and introduction of the highly conductive carbon layer, the NiO/Co$_3$O$_4$@C/CoS$_2$ hybrid electrode exhibits great improvement in electrochemical performance, with a high capacity of ~1025 C g^{-1} at 1 A g^{-1}. Moreover, the NiO/Co$_3$O$_4$@C/CoS$_2$//AC hybrid supercapacitor achieves excellent performance with a maximum voltage of 1.65 V and a high energy density of 62.83 W h kg^{-1} at a power density of 824.99 W kg^{-1} and excellent cycle stability with a capacity retention of ~92% after 5000 cycles. Such binder-free hybrid electrodes with excellent electrochemical performance might hold great potential for use in energy storage devices.

Conflicts of interest

There are no conflicts to declare.

Acknowledgements

Notes and references

1 C. Liu, F. Li, L. P. Ma and H. M. Cheng, *Adv. Mater.*, 2010, **22**, E28–E66.
2 J. R. Miller and P. Simon, *Science*, 2008, **321**, 651–652.
3 C. K. Chan, H. Peng, G. Liu, K. McIlwrath, X. F. Zhang, R. A. Huggins and Y. Cui, *Nat. Nanotechnol.*, 2007, **3**, 651–652.
4 Y. Zhu, S. Murali, M. D. Stoller, K. J. Ganesh, W. Cai, P. J. Ferreira, A. Pirkle, R. M. Wallace, K. A. Cychosz, M. Thommes, D. Su, E. A. Stach and R. S. Ruoff, *Science*, 2011, **332**, 1537–1541.
5 M. Zhi, C. Xiang, J. Li, M. Li and N. Wu, *Nanoscale*, 2013, **5**, 72–88.
6 D. S. Su and R. Schlogl, *ChemSusChem*, 2010, **3**, 136–168.
7 L. L. Zhang and X. S. Zhao, *Chem. Soc. Rev.*, 2009, **38**, 2520–2531.
8 E. Frackowiak and F. Beguin, *Carbon*, 2001, **39**, 937–950.
9 S. S. Zheng, X. R. Li, B. Y. Yan, Q. Hu, Y. X. Xu, X. Xiao, H. G. Xue and H. Pang, *Adv. Energy Mater.*, 2017, **7**, 1602733.
10 S. Faraji and F. N. Ani, *J. Power Sources*, 2014, **263**, 338–360.
11 A. Vlad, N. Singh, C. Galande and P. M. Ajayan, *Adv. Energy Mater.*, 2015, **5**, 1402115.
12 Z. Liang, C. Qu, W. Zhou, R. Zhao, H. Zhang, B. Zhu, W. Guo, W. Meng, Y. Wu, W. Aftab, Q. Wang and R. Zou, *Adv. Sci.*, 2019, **6**, 1802005.

13 Q. Lu, J. G. Chen and J. Q. Xiao, *Angew. Chem., Int. Ed. Engl.*, 2013, **52**, 1882–1889.

14 F. Luan, G. Wang, Y. Ling, X. Lu, H. Wang, Y. Tong, X.-X. Liu and Y. Li, *Nanoscale*, 2013, **5**, 7984–7990.

15 D. M. Zhu and R. A. Miller, *Int. J. Appl. Ceram. Technol.*, 2004, **1**, 86–94.

16 X. Y. Lang, A. Hirata, T. Fujita and M. W. Chen, *Nat. Nanotechnol.*, 2011, **6**, 232–236.

17 W. F. Wei, X. W. Cui, W. X. Chen and D. G. Ivey, *Chem. Soc. Rev.*, 2011, **40**, 1697–1721.

18 Q. Pan, Y. Liu and L. Zhao, *Chem. Eng. J.*, 2018, **351**, 603–612.

19 S. Peng, L. Li, H. Tan, R. Cai, W. Shi, C. Li, S. G. Mhaisalkar, M. Srinivasan, S. Ramakrishna and Q. Yan, *Adv. Funct. Mater.*, 2014, **24**, 2155–2162.

20 H. Tang, J. Wang, H. Yin, H. Zhao, D. Wang and Z. Tang, *Adv. Mater.*, 2015, **27**, 1117–1123.

21 S. H. Lin and J. L. Kuo, *Phys. Chem. Chem. Phys.*, 2015, **17**, 21702–21708.

22 X. Y. Yan, X. L. Tong, L. Ma, Y. M. Tian, Y. S. Cai, C. W. Gong, M. G. Zhang and L. P. Liang, *Mater. Lett.*, 2014, **124**, 133–136.

23 X. H. Wang, H. Y. Xia, X. Q. Wang, B. Shi and Y. Fang, *RSC Adv.*, 2016, **6**, 97482–97490.

24 Q. Chu, W. Wang, X. Wang, B. Yang, X. Liu and J. Chen, *J. Power Sources*, 2015, **276**, 19–25.

25 J. Ning, T. Zhang, Y. He, C. Jia, P. Saha and Q. Cheng, *Materials*, 2017, **10**, 608.

26 Y. Liu, Z. Wang, Y. Zhong, M. Tade, W. Zhou and Z. Shao, *Adv. Funct. Mater.*, 2017, **27**, 1701229.

27 N. Hu, L. Huang, W. Gong and P. K. Shen, *ACS Sustainable Chem. Eng.*, 2018, **6**, 16933–16940.

28 P. Nakhanivej, X. Yu, S. K. Park, S. Kim, J. Y. Hong, H. J. Kim, W. Lee, J. Y. Hwang, J. E. Yang, C. Wolverton, J. Kong, M. Chhowalla and H. S. Park, *Nat. Mater.*, 2019, **18**, 156–162.

29 X. Yu, S. Yun, J. Yeon, P. Bhattacharya, W. Libin, X. Hu and H. S. Park, *Adv. Energy Mater.*, 2018, **8**, 1702930.

30 J. Zhou, Y. B. Dou, A. Zhou, R. M. Guo, M. J. Zhao and J. R. Li, *Adv. Energy Mater.*, 2017, **7**, 1602643.

31 G. H. Li, X. W. Wang, H. Y. Ding and T. Zhang, *RSC Adv.*, 2012, **2**, 13018–13023.

32 S. I. Kim, J. S. Lee, H. J. Ahn, H. K. Song and J. H. Jang, *ACS Appl. Mater. Interfaces*, 2013, **5**, 1596–1603.

33 Y. Sun, C. Liu, D. C. Grauer, J. Yano, J. R. Long, P. Yang and C. J. Chang, *J. Am. Chem. Soc.*, 2013, **135**, 17699–17702.

34 J. C. W. Folmer and D. K. G. de Boer, *Solid State Commun.*, 1981, **38**, 1135–1138.

35 Y. Guo, L. Gan, C. Shang, E. Wang and J. Wang, *Adv. Funct. Mater.*, 2017, **27**, 1602699.

36 M. S. Faber, R. Dziedzic, M. A. Lukowski, N. S. Kaiser, Q. Ding and S. Jin, *J. Am. Chem. Soc.*, 2014, **136**, 10053–10061.

37 A. C. Ferrari, J. C. Meyer, V. Scardaci, C. Casiraghi, M. Lazzeri, F. Mauri, S. Piscanec, D. Jiang, K. S. Novoselov, S. Roth and A. K. Geim, *Phys. Rev. Lett.*, 2006, **97**, 187401.

38 M. S. Dresselhaus, G. Dresselhaus, R. Saito and A. Jorio, *Phys. Rep.*, 2005, **409**, 47–99.

39 Y. Xia, W. Zhang, Z. Xiao, H. Huang, H. Zeng, X. Chen, F. Chen, Y. Gan and X. Tao, *J. Mater. Chem.*, 2012, **22**, 9209–9215.

40 G. M. Zhou, D. W. Wang, L. C. Yin, N. Li, F. Li and H. M. Cheng, *ACS Nano*, 2012, **6**, 3214–3223.

41 E. Anastassakis and C. H. Perry, *J. Chem. Phys.*, 1976, **64**, 3604–3609.

42 L. Q. Mai, A. Minhas-Khan, X. C. Tian, K. M. Hercule, Y. L. Zhao, X. Lin and X. Xu, *Nat. Commun.*, 2013, **4**, 2923.

43 G. P. Anipsitakis, E. Stathatos and D. D. Dionysiou, *J. Phys. Chem. B*, 2005, **109**, 13052–13055.

44 M. Lizer, K. Kozłowska, E. Bobrowska-Grzesik, J. Plewa and H. Altenburg, *Arch. Metall. Mater.*, 2009, **54**, 881–888.

45 H. N. Jia, Z. Y. Wang, C. Li, X. Q. Si, X. H. Zheng, Y. F. Cai, J. H. Lin, H. Y. Liang, J. L. Qi, J. Cao, J. C. Feng and W. D. Fei, *J. Mater. Chem. A*, 2019, **7**, 6686–6694.

46 N. Wang, B. L. Sun, P. Zhao, M. Q. Yao, W. C. Hu and S. Komarneni, *Chem. Eng. J.*, 2018, **345**, 31–38.

47 M. R. Lukatskaya, B. Dunn and Y. Gogotsi, *Nat. Commun.*, 2016, **7**, 13.

48 C. Wei, Y. Huang, M. Chen, J. Yan, W. Yao and X. Chen, *J. Colloid Interface Sci.*, 2017, **504**, 1–11.

49 X. Li, L. Jiang, C. Zhou, J. Liu and H. Zeng, *NPG Asia Mater.*, 2015, **7**, e165.

50 Y. Z. Su, K. Xiao, N. Li, Z. Q. Liu and S. Z. Qiao, *J. Mater. Chem. A*, 2014, **2**, 13845–13853.

51 W. Yang, G. Qu, M. Chen, W. Ma, W. Li and Y. Tang, *Nanotechnology*, 2018, **29**, 295403.

52 F. Cui, Y. Huang, L. Xu, Y. Zhao, J. Lian, J. Bao and H. Li, *Chem. Commun.*, 2018, **54**, 4160–4163.

53 M. Govindasamy, S. Shanthi, E. Elaiyappillai, S. F. Wang, P. M. Johnson, H. Ikeda, Y. Hayakawa, S. Ponnusamy and C. Muthamizhchelvan, *Electrochim. Acta*, 2019, **293**, 328–337.

54 K. H. Oh, G. S. Gund and H. S. Park, *J. Mater. Chem. A*, 2018, **6**, 22106–22114.

55 P. Sivakumar, M. Jana, M. Kota, M. G. Jung, A. Gedanken and H. S. Park, *J. Power Sources*, 2018, **402**, 147–156.